

All-Optically Controlled Memristor for Optoelectronic Neuromorphic Computing

Lingxiang Hu, Jing Yang, Jingrui Wang, Peihong Cheng, Leon O. Chua, and Fei Zhuge*

Neuromorphic computing (NC) is a new generation of artificial intelligence. Memristors are promising candidates for NC owing to the feasibility of their ultrahigh-density 3D integration and their ultralow energy consumption. Compared to traditional electrical memristors, the emerging optoelectronic memristors are more attractive owing to their ability to combine the advantages of both photonics and electronics. However, the inability to reversibly tune the memconductance with light has severely restricted the development of optoelectronic NC. Here, an all-optically controlled (AOC) analog memristor is realized, with memconductance that is reversibly tunable over a continuous range by varying only the wavelength of the controlling light. The device is based on the relatively mature semiconductor material InGaZnO and a memconductance tuning mechanism of light-induced electron trapping and detrapping. It is found that the light-induced multiple memconductance states are nonvolatile. Furthermore, spike-timing-dependent plasticity learning can be mimicked in this AOC memristor, indicating its potential applications in AOC spiking neural networks for highly efficient optoelectronic NC.

to a large extent changes the human life-style. Current practical AI tools are mainly based on deep learning algorithms of artificial neural networks and state-of-the-art hardware systems suffering from the von Neumann bottleneck.^[1] Neuromorphic computing (NC) is considered as the next generation of AI,^[2] which emulates the neural structure and operation of the human brain at the physical level and therefore can perform advanced computing tasks such as learning, recognition, and cognition, in a fast and energy-efficient way.^[3] NC is generally conducted using electronic elements such as complementary metal-oxide-semiconductor integrated circuits,^[4,5] transistors,^[6,7] memristors,^[8–14] and spintronic devices,^[15,16] thus subject to the heat generation and bandwidth limitations. As an alternative, photonic NC has the benefits of high energy-efficiency, low crosstalk and parallel processing,^[17–20] however, it is difficult to achieve high-

density integration of optical devices, and therefore fabricating photonic integrated circuits is a rather complex process.^[21]

Optoelectronic NC based on optoelectronic elements makes possible the combination of the advantages of both photonics and electronics. For an ideal optoelectronic neuromorphic device, e.g., optoelectronic synapse,^[22,23] its weight is represented by conductance that should be all-optically tunable. Various optoelectronic synapses,^[24–36] such as memristive synapses,^[34–36] have recently been developed; however, the device conductance could be reversibly tuned only through a combination of optical and electrical signals. Such an operation scheme makes optoelectronic NC far less attractive. It is worth mentioning that a fully photon-modulated heterostructure was developed,^[33] in which the ultraviolet and infrared light induce long-term synaptic potentiation and short-term synaptic depression behaviors, respectively. In addition, a three-terminal all-optical synapse consisting of two two-terminal devices was reported,^[37] in which one device shows positive photoconductivity upon red light irradiation and the other demonstrates negative photoconductivity upon ultraviolet light irradiation.

Memristors are key candidates for NC because of their unique advantages like very simple structure.^[11] A memristor is generally a two-terminal electronic element with conductance that varies nonlinearly with external stimuli and can be remembered.^[38] Memconductance can be tuned via various mechanisms, such as ion migration,^[39–46] electron trapping,^[47] and phase change.^[48] For optoelectronic memristors

1. Introduction


In the past few years, artificial intelligence (AI) has been getting more and more practical applications to human society, which

L. X. Hu, J. Yang, Dr. J. R. Wang, Prof. P. H. Cheng, Prof. F. Zhuge
Ningbo Institute of Materials Technology and Engineering
Chinese Academy of Sciences
Ningbo 315201, China
E-mail: zhugefei@nimte.ac.cn

L. X. Hu, Prof. F. Zhuge
Center of Materials Science and Optoelectronics Engineering
University of Chinese Academy of Sciences
Beijing 100029, China

Prof. L. O. Chua
Department of Electrical Engineering and Computer Sciences
University of California
Berkeley, CA 94720, USA

Prof. F. Zhuge
Center for Excellence in Brain Science and Intelligence Technology
Chinese Academy of Sciences
Shanghai 200072, China

 The ORCID identification number(s) for the author(s) of this article can be found under <https://doi.org/10.1002/adfm.202005582>.

© 2020 The Authors. Advanced Functional Materials published by Wiley-VCH GmbH. This is an open access article under the terms of the Creative Commons Attribution License, which permits use, distribution and reproduction in any medium, provided the original work is properly cited.

DOI: 10.1002/adfm.202005582

based on electron trapping^[34,49] or proton intercalation,^[35] a light-induced persistent photocurrent^[34,49] or photocatalytic^[35] effect was used to increase the memconductance; however, a decrease in memconductance could be achieved only via electric stimuli^[34,35] or with strong dependence on an external electric field.^[50] In the case of memristors based on conducting nanofilaments (belonging to the class of ion-migration-driven memristors), light illumination can cause filament breakage, resulting in decreased memconductance,^[51,52] however, to increase the memconductance via filament formation or rejuvenation, electric excitation is still necessary.^[51,52] In addition, a photomechanical switching effect can be used to modulate memconductance,^[36] although this causes severe expansion or contraction of the device. To the best of our knowledge, the reversible tuning of memconductance by applying only optical excitation in the same device has not yet been realized.

In this work, we fill this gap by proposing a bilayered oxide memristor based on a memconductance tuning mechanism of electron trapping and detrapping. The memconductance of our device can be reversibly tuned by varying only the wavelength of the controlling light. The light-induced memconductance states are nonvolatile. Our all-optically controlled (AOC) memristor can serve as an excellent synaptic emulator, as we demonstrate by mimicking spike-timing-dependent plasticity (STDP). The realization of AOC neuromorphic devices makes possible real optoelectronic NC that will significantly promote the development of the new generation of AI.

2. Results and Discussion

2.1. Memristive Switching Behavior

In our device, a wide bandgap amorphous oxide material, InGaZnO (IGZO), was used as the active layer. IGZO is widely used as a key thin-film transistor material for high-performance display production. The device is based on an oxygen-deficient IGZO (O_D -IGZO)/oxygen-rich IGZO (O_R -IGZO) homojunction (see the inset of Figure 1a, Experimental Section, and Figure S1 in the Supporting Information). Such a bilayered structure is crucial for achieving an AOC memristor, as will be discussed in detail later. This device demonstrates typical memristive behavior^[53] when measured in the dark (Figure 1a). Positive voltage sweeping converts the device from a low memconductance state (LMS) to a high memconductance state (HMS), referred to as the SET operation; the reverse process of memconductance switching from the HMS to the LMS under negative voltage sweeping is called the RESET operation. The LMS and HMS exhibit nonvolatility (see Figure S2a in the Supporting Information). The memconductance can also be reversibly modulated by alternately applying positive and negative voltage pulses (see Figure S2b in the Supporting Information).

To determine the mechanism of memristive switching, we analyzed the band structures of O_D -IGZO and O_R -IGZO (for details, see the Experimental Section and Figure S3 in the Supporting Information). The analysis indicates that the electrons in O_D -IGZO tend to diffuse into O_R -IGZO, resulting in the formation of a built-in electric field at the O_D -IGZO/ O_R -IGZO interface and, thus, a potential barrier on the O_D -IGZO side and

a potential well on the O_R -IGZO side. The width of this interfacial barrier, which depends on the density of ionized oxygen vacancies (V_O^{2+} s) and determines the tunneling current,^[54,55] plays a key role in memristive switching (for details, see the Experimental Section and Figure S4 in the Supporting Information). Specifically, the SET behavior originates from electron detrapping at neutral oxygen vacancies (V_O s) located in the interfacial barrier region; that is, ionization of the V_O s causes an increase in the density of V_O^{2+} s, thus leading to a decrease in the width of the barrier, which facilitates electron tunneling across the junction (see Figure S4e in the Supporting Information). In contrast, for the RESET behavior, electron trapping at V_O^{2+} s, i.e., the neutralization of V_O^{2+} s, gives rise to an increase in the width of the barrier, thus resulting in a lowered tunneling current (see Figure S4f in the Supporting Information).

2.2. Optical SET Behavior

Having demonstrated memristive behavior under electrical stimulation, we investigated the performance under light exposure. The Au/O_D -IGZO/ O_R -IGZO structure shows a transmittance of >55% for light wavelengths from 400 to 1000 nm (see the inset of Figure S5a in the Supporting Information). Therefore, the device can be irradiated with visible (e.g., 420–650 nm) and near-infrared (e.g., 800–1000 nm) light for memconductance modulation. When the device was measured soon after blue light (420 nm) exposure, we observed memristive behavior similar to that observed in the dark, but with a significant increase in current (Figure 1a). To better understand the influence of irradiation on the memconductance, the effects of irradiating the device using light of various wavelengths (420, 530, 650, 800, 900, and 1000 nm) were investigated (Figure 1b). The current gradually increases under these sub-bandgap illumination conditions. After irradiation, the device exhibits a strong persistent photocurrent. This shows that both visible and near-infrared light can convert the device to a nonvolatile HMS. The light-induced HMS can be reset to the LMS by means of electric stimuli. Thus, the memconductance can be reversibly modulated through a combination of visible (or near-infrared) light and negative voltage pulses (see Figure S5 in the Supporting Information).

Single-layered O_D -IGZO or O_R -IGZO devices exhibit markedly different behavior, which provides insight into the mechanism of optical memconductance. No photocurrent can be observed upon visible light irradiation of the O_D -IGZO device (see Figure S6a in the Supporting Information). For the O_R -IGZO device, a volatile photocurrent is generated upon visible light illumination, but no photocurrent appears upon near-infrared light irradiation (see Figure S6b in the Supporting Information). We therefore deduce that for the bilayered O_D -IGZO/ O_R -IGZO device, the interfacial barrier region plays a key role in the optical SET operation (Figure 1c). Specifically, light-induced transformation from the V_O s located in the interfacial barrier region into V_O^{2+} s causes a decrease in the width of the barrier, thus giving rise to an increased memconductance. The optoelectronic response to near-infrared light indicates the existence of V_O s with energy levels as shallow as 1.24 eV (1000 nm wavelength) below the conduction band of O_D -IGZO, which is supported by photoluminescence measurement, as shown

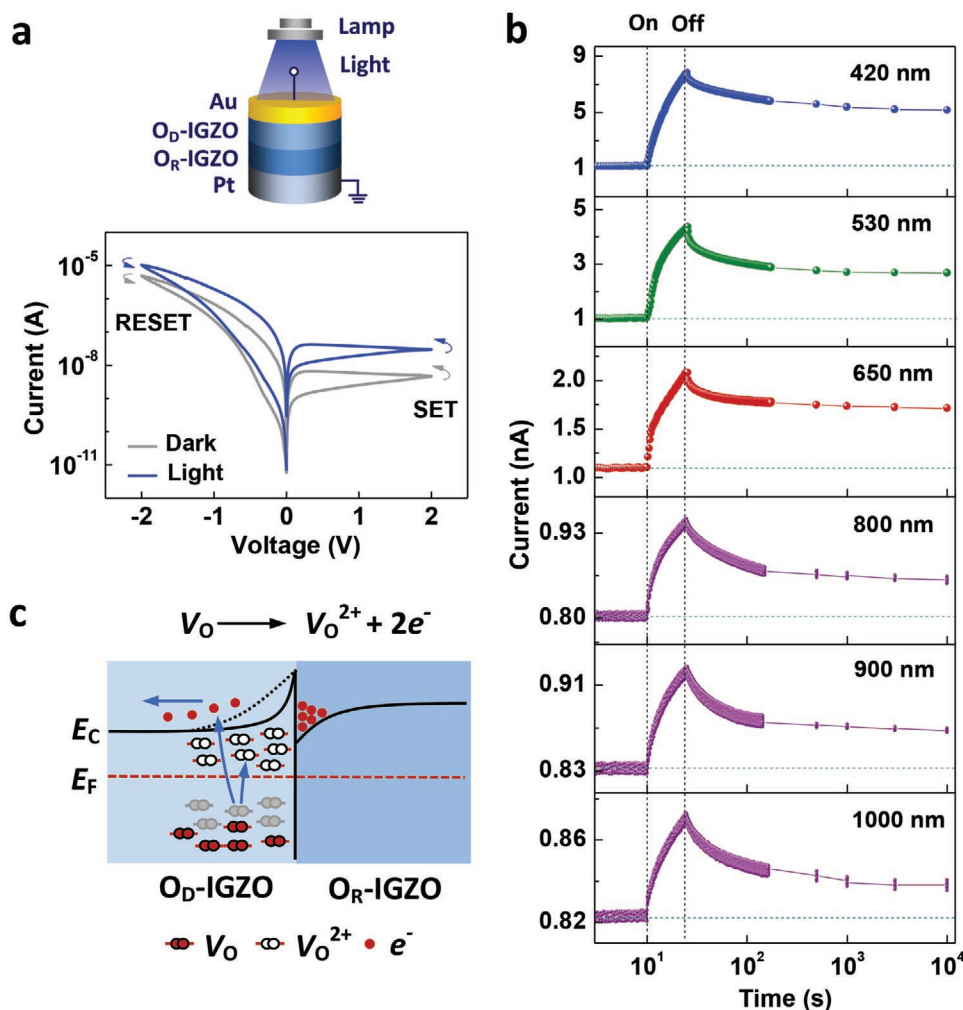


Figure 1. Memristive switching and optical SET behavior. a) Current–voltage characteristics before and after light irradiation (wavelength (λ) = 420 nm, duration (D) = 15 s, and power density (P) = 20 $\mu\text{W cm}^{-2}$). The inset shows a schematic diagram of the measurement configuration. b) Optical SET behavior upon irradiation with light of various wavelengths (D = 15 s and P = 20 $\mu\text{W cm}^{-2}$). The horizontal dashed lines indicate the initial LMS. The vertical dashed lines indicate the times at which the light is switched on and off. The current values were measured at 10 mV. c) Equilibrium energy band diagrams of the O_D-IGZO/O_R-IGZO interface after the optical SET operation. The V₀ ionization (blue arrows) reaction is also schematically illustrated. E_F and E_C denote the Fermi energy and conduction band minimum, respectively. The black dashed lines indicate the positions of E_C before the SET operation. Note that the reaction actually occurs under nonequilibrium conditions.

in Figure S7 in the Supporting Information. In the figure, we can see a broad deep emission band ranging from 500 to >1000 nm centered at 780 nm for O_D-IGZO. It is reported that a high oxygen vacancy density can broaden the energy level distribution of the oxygen vacancies.^[56] When IGZO is deposited in the low oxygen partial pressure environment, the optoelectronic response wavelength can be extended beyond 750 nm.^[57] Given that our O_D-IGZO was deposited in pure argon, we can reasonably deduce that the density of oxygen vacancies in the O_D-IGZO is higher than that in the IGZO deposited in the low oxygen partial pressure environment. Therefore, the O_D-IGZO has a wider energy level distribution of the oxygen vacancies, thus resulting in a longer optoelectronic response wavelength of 1000 nm. The unique long-wavelength response capability of the O_D-IGZO/O_R-IGZO device enables the realization of an AOC memristor.

2.3. Optical RESET Behavior

The key to achieving an AOC memristor is to realize an optical RESET operation. We found that for the blue-light-irradiated device, subsequent irradiation with green (530 nm) and red (650 nm) light causes an increase in the photocurrent after an initial decrease, whereas near-infrared light irradiation (800 and 900 nm) induces a stronger decrease in the current compared to the case without light irradiation (Figure 2a). It indicates that near-infrared light may be used to reset the device irradiated with blue light. To confirm this hypothesis, the device was first exposed to blue light (420 nm) for 15 s to set it to an HMS. Then, it was irradiated with light of various wavelengths from 530 to 900 nm at 10 min after the initial blue light exposure (Figure 2b). Green light (530 nm) converted the device to even higher HMSs, whereas red light (650 nm) resulted in a weak

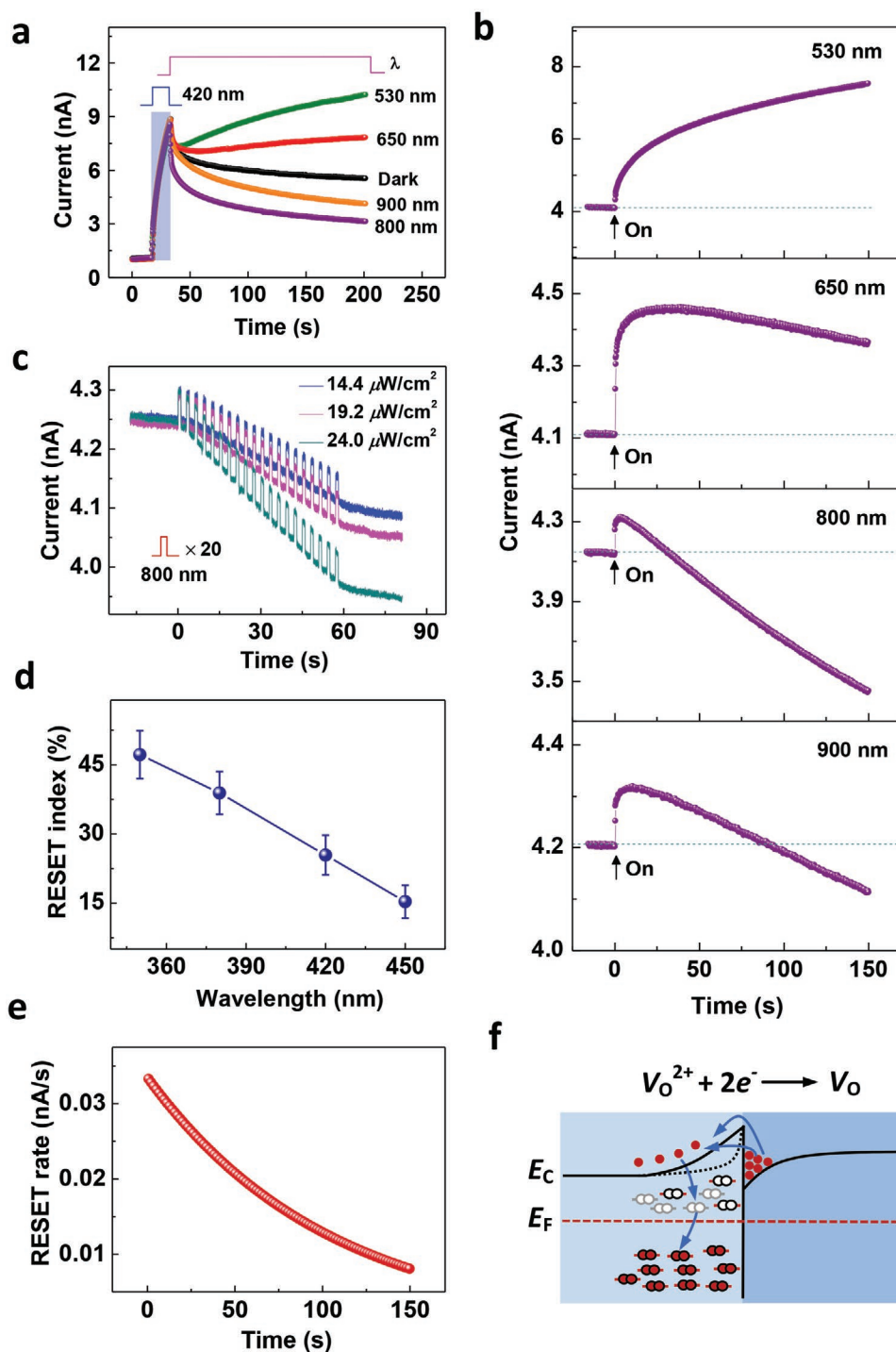


Figure 2. Optical RESET behavior. a) Photocurrent responses to irradiation with light of various wavelengths ($P = 20 \mu\text{W cm}^{-2}$). The device was first exposed to blue light ($D = 15$ s and $P = 20 \mu\text{W cm}^{-2}$). b) Photocurrent responses to irradiation with light of various wavelengths ($P = 20 \mu\text{W cm}^{-2}$). The device was first set to an HMS by blue light irradiation ($D = 15$ s and $P = 20 \mu\text{W cm}^{-2}$), and was then irradiated with light of longer wavelengths 10 min after the initial blue light exposure. The horizontal dashed lines indicate the initial HMS. c) Optical RESET behavior upon exposure to light pulses of various power densities ($D = 1$ s and pulse interval (I) = 2 s). Before applying pulses, the device underwent the same SET operation as in (b). In (a)–(c), the current values were measured at 10 mV. d) Dependence of the RESET index on wavelength of the light used for the initial SET. A part of data is from Figure S9 in the Supporting Information. The RESET index values were calculated by the formula $[(I_1 - I_2)/I_1] \times 100\%$. e) Dependence of the RESET rate on near-infrared light irradiation time. Data are from Figure S9a in the Supporting Information. The RESET rate was calculated by the formula $|c \exp(-t/\tau)|$, where c and τ are constants and t is time. This formula originates from taking the derivative of the function $I = I_0 + I_A \exp(-t/\tau)$. f) Equilibrium energy band diagram after the optical RESET operation. The electron tunneling and jumping and subsequent V_{O}^{2+} neutralization processes that occur upon irradiation are also schematically illustrated (blue arrows). The black dashed lines indicate the positions of E_{C} before the RESET operation. Note that the reaction actually occurs under nonequilibrium conditions.

decrease in the photocurrent after an initial increase. Upon near-infrared light irradiation (800 and 900 nm), a strong decrease in the current, i.e., RESET behavior, was observed following a relatively weak increase; near-infrared light at 800 nm was more efficient than 900 nm light for reducing the device current. Therefore, we selected 800 nm for subsequent RESET operations in pulse mode (Figure 2c). As demonstrated in Figure 2c, the RESET efficiency increased with the light power density.

We also found that the wavelength range for the RESET operation strongly depends on the light used for the initial SET operation. After ultraviolet light illumination (350 nm), the device can be reset to an LMS by both red and near-infrared light (see Figure S8a in the Supporting Information). However, a device irradiated with green or red light cannot be restored to the LMS even by near-infrared light (see Figure S8b,c in the Supporting Information). Moreover, the ultraviolet-light-illuminated device (see Figure S8a in the Supporting Information) exhibits a current reduction of a larger magnitude upon near-infrared light irradiation than the blue-light-exposed device in Figure 2b. These findings suggest that setting the device with short-wavelength light facilitates the subsequent RESET operation. To further confirm this conclusion, the initial SET was performed with 350, 380, 420, and 450 nm light, followed by a RESET operation with 800 nm light (see Figure S9 in the Supporting Information). Figure 2d illustrates the RESET indexes for different SET operations, which quantitatively represent the RESET efficiency. Obviously, RESET index decreases with increasing wavelength of the light for the SET operation. Then, we can safely conclude that the shorter the light wavelength during the SET operation, the better the subsequent RESET operation. The RESET rate, which represents the instantaneous rate of memconductance decrease, was found to decrease with irradiation time (Figure 2e).

Because the optical SET mechanism depends on barrier narrowing (Figure 1c), we expected that widening of the barrier region due to a reduced V_O^{2+} density would result in an optical RESET. Upon near-infrared light irradiation, electrons in the potential well formed by band bending of O_R -IGZO are apt to tunnel through^[58] or jump over^[59] the barrier and enter the O_D -IGZO conduction band (Figure 2f). Some electrons are captured by V_O^{2+} s, which then transform into V_O s. This explanation for the RESET mechanism can be supported by the strong dependence of the RESET efficiency on the light power density in Figure 2c; that is, light with a higher power density excites

more electrons into the conduction band of O_D -IGZO, leading to a larger probability of V_O^{2+} neutralization and thus widening the interfacial barrier.

We further propose that upon illumination, these two opposite reactions, namely, the ionization of V_O s and the neutralization of V_O^{2+} s, occur simultaneously. The photocurrent depends on the dynamic equilibrium between these two reactions. In the ionization-dominated (or neutralization-dominated) case, the device shows an increase (or decrease) in photocurrent. For a device in the LMS, the ionization of V_O s is dominant, thus resulting in an increase in memconductance upon light irradiation (Figure 1b). However, when the device is initially exposed to light of a relatively short wavelength, only a small number of V_O s can be ionized by subsequent irradiation at a longer wavelength owing to the low density of V_O s with relatively shallow energy levels. In this case, the neutralization of V_O^{2+} s may dominate, enabling a decrease in the memconductance (Figure 2b,c; Figures S8a,b and S9, Supporting Information). The increase (or initial increase) in the memconductance observed in Figure 2b,c, Figures S8 and S9 (Supporting Information) most likely originates from the ionization of V_O s regenerated from the spontaneous neutralization of V_O^{2+} s by electron tunneling through the interfacial barrier. This spontaneous transformation from V_O^{2+} s to V_O s gives rise to the persistent photocurrent decay that was seen in Figure 1b. Based on the above discussion, the actual optical SET and RESET processes are schematically illustrated in Figure 3. The existence of a competitive relationship between the ionization of V_O s and the neutralization of V_O^{2+} s can be supported by the strong dependence of the RESET efficiency on the light wavelength for the initial SET operation in Figure 2d and the decreasing RESET rate with light irradiation time in Figure 2e. In the former case, light with a shorter wavelength transforms more V_O s into V_O^{2+} in O_D -IGZO. During the subsequent RESET operation, the infrared light transforms less V_O s into V_O^{2+} , leading to a higher RESET efficiency. In the latter case, the V_O density in O_D -IGZO increases with irradiation time, resulting in an increasing probability of V_O ionization and thus decreasing the RESET rate.

2.4. AOC Memristor

We implemented our bilayered O_D -IGZO/ O_R -IGZO memristor using blue and near-infrared light pulses for the SET

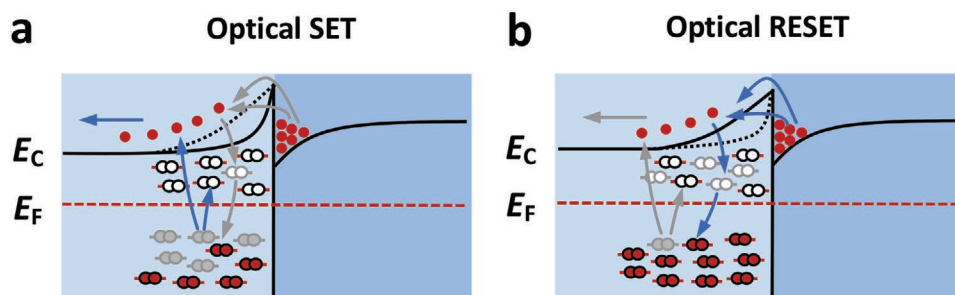


Figure 3. Schematic illustrations of the competitive relationship between oxygen vacancy ionization and neutralization upon light irradiation. a) Optical SET. b) Optical RESET. The reaction marked by blue arrows plays a dominating role in the optoelectronic response and the reaction marked by gray arrows is nondominating.

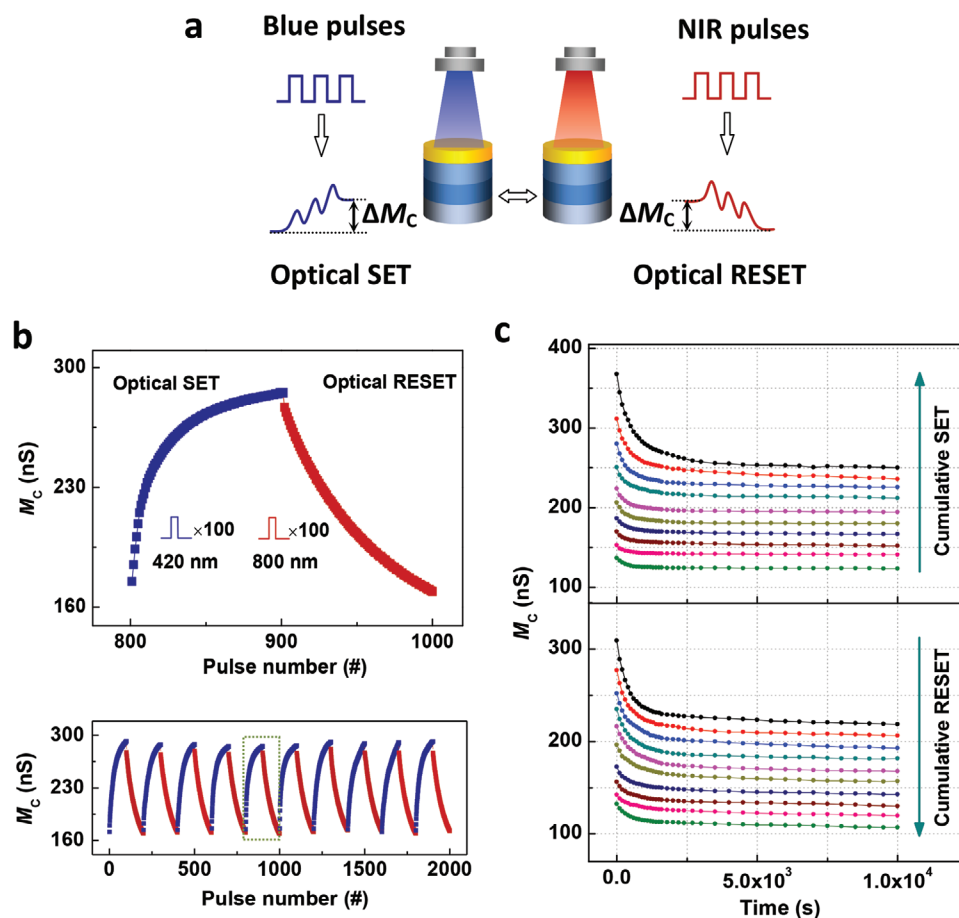


Figure 4. AOC memristor. a) Schematic of the realization of an AOC memristor. M_c and NIR denote the memconductance and near-infrared, respectively. b) Top panel: Reversible regulation of the memconductance by means of 100 blue light pulses ($D = 1$ s, $I = 1$ s, and $P = 20 \mu\text{W cm}^{-2}$) and 100 NIR light pulses ($D = 1$ s, $I = 1$ s, and $P = 24 \mu\text{W cm}^{-2}$). Bottom panel: Ten successive memconductance increase–decrease cycles. The top panel shows an enlarged view of the fifth cycle, as marked by the green rectangle in the bottom panel. The memconductance values were measured 1 s after each light pulse. c) Retention characteristics of ten memconductance states after both optical SET (top panel) and optical RESET (bottom panel) operations. Top panel: The device was initially set to a relatively low memconductance of about 100 nS, and then ten SET operations were performed with different numbers of 420 nm light pulses. After each SET operation and subsequent retention measurement, the device was set to 100 nS again. Bottom panel: The device was initially set to a relatively high memconductance of about 400 nS, and then ten RESET operations were conducted with different numbers of 800 nm light pulses. After each RESET operation and subsequent retention measurement, the device was set to 400 nS again. In (b) and (c), the memconductance values were measured at 10 mV.

and RESET processes, respectively, as schematically illustrated in Figure 4a. The top panel in Figure 4b shows a continuous increase and decrease in the memconductance under a series of successive light pulses. Our AOC memristor exhibits good operation endurance (Figure 4b, bottom panel). To verify the nonvolatility of the light-induced memconductance states, we present retention measurements of ten states obtained after both the SET and RESET operations (Figure 4c). The memconductance exhibits an initial slow decay, which is an intrinsic feature of optoelectronic devices,^[23–35,49,55] and then remains stable, with all states being clearly distinguishable even after 10^4 s. The retention measurement results indicate that the light-induced memconductance states are nonvolatile regardless of the operation mode (SET or RESET).

As mentioned above, the persistent photocurrent decay is related to the tunneling of electrons through the interfacial barrier, which is why the decay was weaker for lower

memconductance. More specifically, a lower memconductance implies a wider barrier, resulting in fewer electrons tunneling through it. Subsequently, fewer V_O^{2+} s transform into V_O s, thus leading to less barrier widening.

Our AOC memristor is structure-changeable. For example, Pt and Ti can also be used as the top electrode. Pt/ O_D -IGZO/ O_R -IGZO/Pt and Ti/ O_D -IGZO/ O_R -IGZO/Pt demonstrate similar optoelectronic behaviors to Au/ O_D -IGZO/ O_R -IGZO/Pt (see Figure S10 in the Supporting Information). Apart from metals, a transparent conducting oxide (Sn-doped In_2O_3 (ITO)) can also serve as the top electrode. The ITO/ O_D -IGZO/ O_R -IGZO/Pt shows electrical and optoelectronic behavior similar to that of Au/ O_D -IGZO/ O_R -IGZO/Pt (see Figure S11 in the Supporting Information). Given that O_D -IGZO is highly conductive and thus Ohmic contact forms in the top electrode/ O_D -IGZO interface (see Figure S4a in the Supporting Information), similar electrical and optoelectronic behaviors could

be expected when using other metals or conducting oxides as the top electrode.

We have also tried employing other oxides, such as ZnO, In_2O_3 and SnO_2 , as the active layer of memristive devices with the same structure as that of IGZO, i.e., Au/oxygen-deficient oxide (O_D -oxide)/oxygen-rich oxide (O_R -oxide)/Pt. However, no optical RESET behavior could be realized in these memristors. It may be due to 1) a weak persistent photocurrent and 2) a poor long-wavelength response capability, for example, no optoelectronic response was observed upon the light irradiation with wavelength >700 nm. We will try other ternary and quaternary oxides or modifying the deposition parameters of binary oxides. We want to check if optical RESET behavior exists in memristive devices with other materials (other than IGZO) as the active layer.

2.5. AOC Memristive Synapse

The multiple reversibly tunable memconductance states of our AOC memristor (Figure 4b) make it an excellent synaptic emulator. Specifically, we found that our memristor can mimic STDP—an important learning rule in the brain that requires variation in the synaptic weight (W) to be a strong function of the pre- and postsynaptic spike timing (Δt)^[60] (Figure 5a). A single blue light pulse and a train of ten near-infrared light pulses serve as pre- and postsynaptic spikes, respectively (Figure 5a, inset). The memconductance is denoted as W . We see that synaptic potentiation ($\Delta W > 0$) occurs when the pre-synaptic spike arrives before the postsynaptic spike ($\Delta t > 0$); by contrast, synaptic depression ($\Delta W < 0$) occurs when the post-synaptic spike arrives first ($\Delta t < 0$). In addition, $|\Delta W|$ increases with decreasing $|\Delta t|$. These observations are consistent with the typical STDP characteristics of biological synapses.^[60] Given that STDP is the basic learning rule of spiking neural networks (SNNs) that reflect the information processing style in the human brain,^[61] our AOC memristor is promising for applications in optoelectronic SNNs.

The mechanism of STDP emulation is explained in detail in Figure 5b,c. For the emulation of synaptic potentiation, the device was initially set to a relatively low memconductance of $M_{C0} \approx 100$ nS. Figure 5b presents two W modulation events with $\Delta t_2 > \Delta t_1 > 0$. First, the blue light pulse induces a positive persistent photoconductance, that is, a light-induced memconductance that is higher than M_{C0} . The subsequent near-infrared light pulses induce a negative persistent photoconductance, that is, a light-induced memconductance that is lower than that before near-infrared irradiation. We can see from Figure 5b that the updated memconductance (M_{C1} or M_{C2}) is higher than M_{C0} , indicating the realization of synaptic potentiation. Given that $\Delta t_1 < \Delta t_2$, the M_C values before and after near-infrared light irradiation for Δt_1 are higher than those for Δt_2 . It follows that $M_{C1} > M_{C2}$, and thus, $\Delta W_1 > \Delta W_2$. To mimic synaptic depression, the device was initially set to a relatively high memconductance of $M_{C0} \approx 250$ nS. Figure 5c shows two W modulation events with $\Delta t_2 < \Delta t_1 < 0$. First, the near-infrared light pulses induce a negative persistent photoconductance. The subsequent blue light pulse induces a positive persistent photoconductance. The updated memconductance (M_{C1} or M_{C2}) is lower

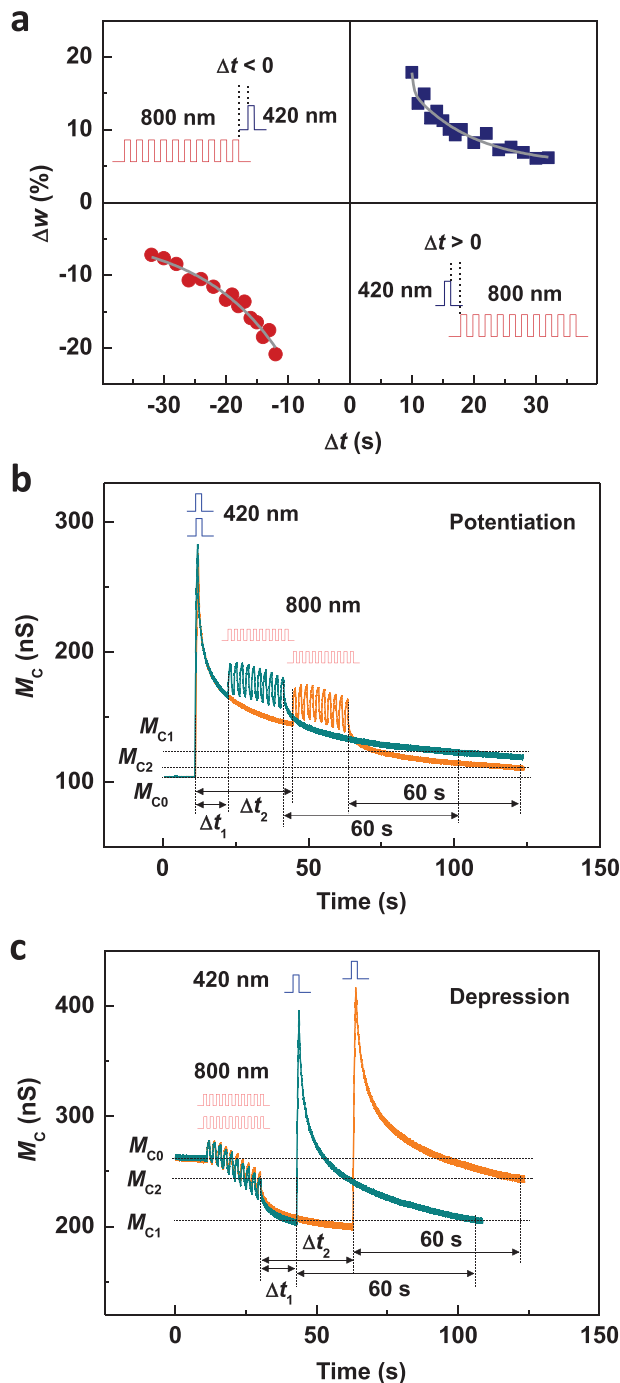


Figure 5. AOC memristive synapse. a) Emulation of synaptic STDP in the AOC memristor. The insets illustrate the light pulse schemes. b,c) Mechanism of STDP emulation. M_{C0} is the initial memconductance value, and M_{C1} and M_{C2} are the updated values that are measured 60 s after the spikes. The synaptic weight variation was calculated using the following formula: $\Delta W_i = [(M_{Ci} - M_{C0})/M_{C0}] \times 100\%$, where $i = 1$ and 2. In (a)–(c), the memconductance values were measured at 10 mV.

than M_{C0} , indicating the realization of synaptic depression. Given that $|\Delta t_1| < |\Delta t_2|$, the memconductance before blue light irradiation for Δt_1 is higher than that for Δt_2 . However, because of the relatively large decay amplitude of the memconductance

after blue light irradiation, the subsequent memconductance for Δt_1 is lower than that for Δt_2 . Therefore, $M_{C1} < M_{C2}$ and $|\Delta W_1| > |\Delta W_2|$.

It deserves mention that choosing an appropriate number of near-infrared light pulses is crucial for mimicking STDP. It is found that ten is the optimal choice for achieving both synaptic potentiation and depression. When too few/too many near-infrared light pulses are used, only synaptic potentiation/depression can be obtained regardless of Δt . Figure S12 in the Supporting Information illustrates the effect of the number of near-infrared light pulses on the STDP emulation. It can be seen that the application of five near-infrared light pulses results in synaptic potentiation even when $\Delta t < 0$, whereas the application of twenty near-infrared light pulses leads to synaptic depression even when $\Delta t > 0$.

3. Conclusions

We believe that the realization of AOC memristors is an important milestone toward real optoelectronic NC that possesses the advantages of both photonics and electronics. For traditional electrical memristors, a high voltage or current is generally required to tune their memconductance. Such strong electrical stimuli may result in 1) high power consumption, 2) a large amount of Joule heat, 3) microstructural change accelerated by the Joule heat, and 4) high crosstalk in memristor crossbars. These issues can be addressed with our AOC memristor given the very low light power densities ($\approx 20 \mu\text{W cm}^{-2}$) required to operate it. On the other hand, optoelectronic computing using our AOC memristor is more practically feasible than purely optical computing^[18–20] owing to the simple structure and easy fabrication of this device. Future research might explore neuronal functions (e.g., integrate and fire) using our AOC memristor to enable optoelectronic SNNs.

4. Experimental Section

Material Growth: Amorphous IGZO thin films with a diameter of 100 μm were deposited on Pt/Ti/SiO₂/Si, SiO₂/Si, and quartz substrates at room temperature (RT) via RF magnetron sputtering of an InGaZnO₄ (In₂O₃:Ga₂O₃:ZnO = 1:1:2, molar ratio) ceramic target of 99.99% purity with in situ metal shadow masks. The sputtering power and pressure were 60 W and 0.5 Pa, respectively. O_D-IGZO was sputtered in pure Ar gas, and O_R-IGZO was deposited in a mixed Ar and O₂ atmosphere with a partial pressure ratio of 1:1. The thickness of the O_D-IGZO and O_R-IGZO films was ≈ 30 nm. For the fabrication of O_D-IGZO/O_R-IGZO homojunctions, O_R-IGZO was sputtered first, followed by deposition of O_D-IGZO.

Device Fabrication: 10 nm thick Au top electrodes with a diameter of 100 μm were deposited onto O_D-IGZO, O_R-IGZO, and O_D-IGZO/O_R-IGZO films at RT via electron-beam evaporation with in situ metal shadow masks. ITO electrodes with a thickness of 30 nm and a diameter of 100 μm were deposited at RT via RF magnetron sputtering of an ITO (In₂O₃:SnO₂ = 5:1, molar ratio) ceramic target of 99.99% purity with in situ metal shadow masks. Ar gas was used as the sputtering atmosphere. The sputtering power and pressure were 40 W and 0.5 Pa, respectively.

Electrical and Optoelectronic Characterization: Electrical and optoelectronic measurements were performed at RT in air using a Keithley 4200 semiconductor parameter analyzer equipped with a

monochromatic light source (Omni- λ 3007). The bias voltage was applied to the top electrode (Au or ITO) with the bottom electrode (Pt) grounded, and the light entered into the device through the top electrode (Au or ITO) (Figure 1a).

It is found that the as-fabricated bilayered O_D-IGZO/O_R-IGZO device was not in an LMS but in an HMS with a memconductance of $\approx 10^2$ – 10^3 nS (at -10 mV). Given that the device was highly sensitive to visible light and that exposure to environmental light was inevitable, such an HMS should be induced by environmental light exposure. To restore the device to the initial LMS before electrical or optoelectronic measurements, an electrical or optical RESET operation was first performed. After the RESET operation, the device presented a low memconductance of approximately 10^{-1} – 10^2 nS (at -10 mV) depending on the RESET parameters used.

Material Characterization: The film thickness was measured via variable angle spectroscopic ellipsometry (M-2000 DI, J. A. Woollam Co., Inc.). The carrier density and resistivity were determined with a Hall effect measurement system (HP-5500C, Nanometrics) using the van der Pauw method. Absorption and transmittance spectra were collected using both a UV–vis–IR spectrophotometer (Lambda 950, PerkinElmer) and spectroscopic ellipsometry. Photoluminescence spectra were measured with a confocal microscopic Raman spectrometer (Renishaw inVia Reflex, 325 nm). All of the above measurements were performed at RT in air. Cross-sectional microstructural observations were performed by means of high-resolution transmission electron microscopy (HRTEM, Talos F200X, Thermo Fisher). Cross-sectional specimens were fabricated by means of focused ion beam etching. Elemental and energy-band structure analyses were conducted using X-ray photoelectron spectroscopy (XPS, Kratos Axis Ultra DLD). The work function was determined via ultraviolet photoelectron spectroscopy (UPS). O_D-IGZO and O_R-IGZO films with a thickness of 100 nm were used for the XPS and UPS measurements. To eliminate the influence of surface contamination (e.g., moisture from the atmosphere) on the measurements, an ≈ 30 nm thick surface layer was etched with Ar plasma before the optoelectronic signals were collected.

The HRTEM images and corresponding fast Fourier transform (FFT) images revealed the amorphous structures of O_D-IGZO and O_R-IGZO (Figure S1 in the Supporting Information). From the XPS measurements, the molar ratios of In:Ga:Zn:O for the O_D-IGZO and O_R-IGZO were estimated to be 1.2:2.2:1:4.5 and 1.2:2.1:1:4.6, respectively.

As determined by Hall effect measurements, O_D-IGZO showed an electron concentration of 10^{19} cm^{-3} and a resistivity of $10^{-2} \Omega \text{ cm}$. O_R-IGZO had a much higher resistivity, which exceeded the measurement limit ($\approx 10^5 \Omega \text{ cm}$) of the Hall measurement system. Given that oxygen vacancies are the main n-type dopants in IGZO,^[62] the low resistivity of the O_D-IGZO indicates a high density of oxygen vacancies. The lower conductivity of O_R-IGZO indicates that it contains much fewer oxygen vacancies than O_D-IGZO. The oxygen vacancies in IGZO have a wide distribution of energy levels in the bandgap.^[63–65]

Band Structure Analysis: The optical bandgaps (E_g) of O_D-IGZO and O_R-IGZO were determined to be 3.7 and 3.6 eV, respectively, via a modified Kubelka–Munk function (Figure S3a in the Supporting Information). The E_g values were obtained from the abscissa intercepts of the straight lines fitted to the linear portions of the plotted data points in the high energy region.

The differences between the Fermi energy (E_F) and the valence band maximum (E_V) for O_D-IGZO and O_R-IGZO were determined to be 3.1 and 2.5 eV, respectively, by measuring the valence band XPS spectra (Figure S3b in the Supporting Information). The values were obtained from the positions of the intersections of the straight lines fitted to the leading edges of the spectra and the straight lines fitted to the flat energy distribution portions in the low energy region.

The work functions (Φ) of O_D-IGZO and O_R-IGZO were determined to be 4.2 and 4.9 eV, respectively, by measuring the valence band UPS spectra (He I, 21.22 eV) (Figure S3c in the Supporting Information). The position of the secondary electron cutoff (E_{cutoff}) was determined from the midpoint of the cutoff edge. Φ could then be calculated as $\Phi = h\nu - E_{\text{cutoff}}$, where h is the Planck constant, ν is the frequency of the light,

and $h\nu$ is the photon energy (21.22 eV). The differences between E_F and E_V for O_D -IGZO and O_R -IGZO were determined to be 3.2 and 2.6 eV, respectively, which are consistent with the values obtained from the XPS spectra (Figure S3b in the Supporting Information).

Then, the energy band diagrams of O_D -IGZO and O_R -IGZO can be plotted before contact, as shown in Figure S3d (Supporting Information). The differences between the conduction band minimum (E_C) and E_F for O_D -IGZO and O_R -IGZO were calculated to be 0.6 and 1.1 eV, respectively, according to $E_g - (E_F - E_V)$. Subsequently, the differences between the vacuum energy (E_{VAC}) and E_C for O_D -IGZO and O_R -IGZO were determined to be 3.6 and 3.8 eV, respectively, according to $\Phi - [E_g - (E_F - E_V)]$.

After contact, the Fermi levels of O_D -IGZO and O_R -IGZO tend to equilibrate via electron transfer from O_D -IGZO to O_R -IGZO (Figure S3e in the Supporting Information), resulting in the formation of positive space charges (ions) on the O_D -IGZO side and negative space charges (electrons) on the O_R -IGZO side and thus a built-in electric field at the O_D -IGZO/ O_R -IGZO interface (Figure S3f in the Supporting Information). As a consequence, the energy band is bent upward on the O_D -IGZO side and downward on the O_R -IGZO side; that is, a potential barrier is formed on the O_D -IGZO side, and a potential well is formed on the O_R -IGZO side (Figure S3e in the Supporting Information).

Analysis of the Memristive Switching Mechanism: Given the pronounced difference in current–voltage (I – V) characteristics between a bilayered O_D -IGZO/ O_R -IGZO device (Figure 1a) and a single-layered O_D -IGZO or O_R -IGZO device (Figure S4a,b in the Supporting Information), it is deduced that the O_D -IGZO/ O_R -IGZO interfacial region plays a key role in memristive switching. Moreover, the strong dependence of the memconductance on the device size (i.e., the diameter of the top electrode or IGZO thin film) for both HMSs and LMSs indicates radially homogeneous switching behavior^[66] (Figure S4c in the Supporting Information). It is therefore proposed that the memristive switching of a bilayered O_D -IGZO/ O_R -IGZO device originates from electron trapping (or detrapping) at ionized (or neutral) oxygen vacancies (V_O^{2+} s or V_O s) located in the O_D -IGZO/ O_R -IGZO interfacial barrier region (Figure S4e,f in the Supporting Information). This proposal is consistent with the memconductance tuning mechanism upon light irradiation.

More specifically, it is proposed that the memconductance of the device mainly depends on the width of the O_D -IGZO/ O_R -IGZO interfacial barrier, which determines the tunneling current.^[54,55] The barrier width is determined by the density of positive ion space charges (i.e., ionized oxygen vacancies): a higher density of ionized oxygen vacancies results in a narrower barrier width.^[54] As mentioned above, there are abundant V_O s with a wide distribution of energy levels in O_D -IGZO. The V_O s in relatively shallow energy states tend to be doubly ionized,^[67,68] transforming into V_O^{2+} s with shallow energy levels (Figure S4d in the Supporting Information). When a positive bias is applied to the device, some of the V_O s in relatively deep energy states ionize into V_O^{2+} s^[69] (Figure S4e in the Supporting Information). These additional V_O^{2+} s generated in the barrier region cause the barrier to narrow, which facilitates electron tunneling across the junction. Thus, the device is set to an HMS. The HMS is nonvolatile because free electrons produced in the barrier region are swiftly pulled into O_D -IGZO by either the built-in or the external electric field and therefore cannot recombine with V_O^{2+} s. The existence of an energy barrier hindering V_O^{2+} neutralization also contributes to the nonvolatility.^[67] When a negative voltage is applied, the interfacial barrier is forward biased, and many electrons are injected into the barrier region. Some electrons will be captured by V_O^{2+} s generated during the electrical SET operation, which then transform back into V_O s (Figure S4f in the Supporting Information). As a result, the barrier becomes wide again and the device is reset to the LMS.

The current decay of the HMS in Figure S2a (Supporting Information) can therefore be explained by the spontaneous neutralization of ionized oxygen vacancies: some electrons tunneling through the interfacial barrier from O_R -IGZO to O_D -IGZO are captured by ionized oxygen vacancies, which then transform into neutral oxygen vacancies; a decrease in the number of ionized oxygen vacancies results in widening of the interfacial barrier and, thus, a reduction in current.

Supporting Information

Supporting Information is available from the Wiley Online Library or from the author.

Acknowledgements

This work was supported in part by the National Natural Science Foundation of China (Nos. 61674156 and 61874125), the Strategic Priority Research Program of Chinese Academy of Sciences (No. XDB32050204), the Zhejiang Provincial Natural Science Foundation of China (No. LD19E020001), and the Ningbo Natural Science Foundation of China (No. 2018A610019).

Conflict of Interest

The authors declare no conflict of interest.

Keywords

all-optically controlling, memristive synapses, neuromorphic computing, optoelectronic memristors

Received: July 3, 2020

Revised: September 18, 2020

Published online: November 20, 2020

- [1] Q. Xia, J. J. Yang, *Nat. Mater.* **2019**, *18*, 309.
- [2] Neuromorphic Computing: Beyond Today's AI, <https://www.intel.com/content/www/us/en/research/neuromorphic-computing.html> (accessed: May 2020).
- [3] D. Ielmini, *Microelectron. Eng.* **2018**, *190*, 44.
- [4] C. Mead, *Proc. IEEE* **1990**, *78*, 1629.
- [5] P. A. Merolla, J. V. Arthur, R. Alvarez-Icaza, A. S. Cassidy, J. Sawada, F. Akopyan, B. L. Jackson, N. Imam, C. Guo, Y. Nakamura, B. Brezzo, I. Vo, S. K. Esser, R. Appuswamy, B. Taba, A. Amir, M. D. Flickner, W. P. Risk, R. Manohar, D. S. Modha, *Science* **2014**, *345*, 668.
- [6] C. Diorio, P. Hasler, B. A. Minch, C. A. Mead, *IEEE Trans. Electron Devices* **1996**, *43*, 1972.
- [7] E. J. Fuller, S. T. Keene, A. Melianas, Z. Wang, S. Agarwal, Y. Li, Y. Tuchman, C. D. James, M. J. Marinella, J. J. Yang, A. Salleo, A. A. Talin, *Science* **2019**, *364*, 570.
- [8] S. H. Jo, T. Chang, I. Ebong, B. B. Bhadviya, P. Mazumder, W. Lu, *Nano Lett.* **2010**, *10*, 1297.
- [9] S. Yu, Y. Wu, R. Jayasingh, D. Kuzum, H.-S. P. Wong, *IEEE Trans. Electron Devices* **2011**, *58*, 2729.
- [10] R. Yang, K. Terabe, G. Liu, T. Tsuruoka, T. Hasegawa, J. K. Gimzewski, M. Aono, *ACS Nano* **2012**, *6*, 9515.
- [11] M. Prezioso, F. Merrikh-Bayat, B. D. Hoskins, G. C. Adam, K. K. Likharev, D. B. Strukov, *Nature* **2015**, *521*, 61.
- [12] Z. Wang, S. Joshi, S. Savel'ev, W. Song, R. Midya, Y. Li, M. Rao, P. Yan, S. Asapu, Y. Zhuo, H. Jiang, P. Lin, C. Li, J. H. Yoon, N. K. Upadhyay, J. Zhang, M. Hu, J. P. Strachan, M. Barnell, Q. Wu, H. Wu, R. S. Williams, Q. Xia, J. J. Yang, *Nat. Electron.* **2018**, *1*, 137.
- [13] B. Li, Y. Q. Liu, C. J. Wan, Z. Y. Liu, M. Wang, D. P. Qi, J. C. Yu, P. Q. Cai, M. Xiao, Y. Zeng, X. D. Chen, *Adv. Mater.* **2018**, *30*, 1706395.
- [14] P. Yao, H. Wu, B. Gao, J. Tang, Q. Zhang, W. Zhang, J. J. Yang, H. Qian, *Nature* **2020**, *577*, 641.
- [15] A. Sengupta, Z. Al Azim, X. Fong, K. Roy, *Appl. Phys. Lett.* **2015**, *106*, 093704.

- [16] J. Torrejon, M. Riou, F. A. Araujo, S. Tsunegi, G. Khalsa, D. Querlioz, P. Bortolotti, V. Cros, K. Yakushiji, A. Fukushima, H. Kubota, S. Y. Uasa, M. D. Stiles, J. Grollier, *Nature* **2017**, 547, 428.
- [17] H. J. Caulfield, S. Dolev, *Nat. Photonics* **2010**, 4, 261.
- [18] X. Lin, Y. Rivenson, N. T. Yardime, M. Veli, Y. Luo, M. Jarrahi, A. Ozcan, *Science* **2018**, 361, 1004.
- [19] J. Feldmann, N. Youngblood, C. D. Wright, H. Bhaskaran, W. H. P. Pernice, *Nature* **2019**, 569, 208.
- [20] H.-T. Peng, M. A. Nahmias, T. F. de Lima, A. N. Tait, B. J. Shastri, P. R. Prucnal, *IEEE J. Sel. Top. Quantum Electron.* **2018**, 24, 6101715.
- [21] X. Zhuge, J. Wang, F. Zhuge, *Phys. Status Solidi RRL* **2019**, 13, 1900082.
- [22] J. Zhu, T. Zhang, Y. Yang, R. Huang, *Appl. Phys. Rev.* **2020**, 7, 011312.
- [23] J.-Y. Mao, L. Zhou, X. Zhu, Y. Zhou, S.-T. Han, *Adv. Opt. Mater.* **2019**, 7, 1900766.
- [24] Y. Lee, J. Y. Oh, W. Xu, O. Kim, T. R. Kim, J. Kang, Y. Kim, D. Son, J. B.-H. Tok, M. J. Park, Z. Bao, T.-W. Lee, *Sci. Adv.* **2018**, 4, eaat7387.
- [25] H. Tan, Z. Ni, W. Peng, S. Du, X. Liu, S. Zhao, W. Li, Z. Ye, M. Xu, Y. Xu, X. Pi, D. Yang, *Nano Energy* **2018**, 52, 422.
- [26] S. Seo, S.-H. Jo, S. Kim, J. Shim, S. Oh, J.-H. Kim, K. Heo, J.-W. Choi, C. Choi, S. Oh, D. Kuzum, H.-S. P. Wong, J.-H. Park, *Nat. Commun.* **2018**, 9, 5106.
- [27] Y. He, S. Nie, R. Liu, S. Jiang, Y. Shi, Q. Wan, *IEEE Electron Device Lett.* **2019**, 40, 818.
- [28] S. Wang, C. Chen, Z. Yu, Y. He, X. Chen, Q. Wan, Y. Shi, D. W. Zhang, Z. Zhou, X. Wang, P. Zhou, *Adv. Mater.* **2019**, 31, 1806227.
- [29] R. A. John, F. Liu, N. A. Chien, M. R. Kulkarni, C. Zhu, Q. Fu, A. Basu, Z. Liu, N. Mathews, *Adv. Mater.* **2018**, 30, 1800220.
- [30] T. Ahmed, S. Kuriakose, E. L. H. Mayes, R. Ramanathan, V. Bansal, M. Bhaskaran, S. Srim, S. Walia, *Small* **2019**, 15, 1900966.
- [31] M. Lee, W. Lee, S. Choi, J.-W. Jo, J. Kim, S. K. Park, Y.-H. Kim, *Adv. Mater.* **2017**, 29, 1700951.
- [32] N. Duan, Y. Li, H.-C. Chiang, J. Chen, W.-Q. Pan, Y.-X. Zhou, Y.-C. Chien, Y.-H. He, K.-H. Xue, G. Liu, T.-C. Chang, X.-S. Miao, *Nanoscale* **2019**, 11, 17590.
- [33] H. L. Li, X. T. Jiang, W. B. Ye, H. Zhang, L. Zhou, F. Zhang, D. H. She, Y. Zhou, S.-T. Han, *Nano Energy* **2019**, 65, 104000.
- [34] D. C. Hu, R. Yang, L. Jiang, X. Guo, *ACS Appl. Mater. Interfaces* **2018**, 10, 6463.
- [35] F. Zhou, Z. Zhou, J. Chen, T. H. Choy, J. Wang, N. Zhang, Z. Lin, S. Yu, J. Kang, H.-S. Philip Wong, Y. Chai, *Nat. Nanotechnol.* **2019**, 14, 776.
- [36] A. H. Jaafar, M. O'Neill, S. M. Kelly, E. Verrelli, N. T. Kemp, *Adv. Electron. Mater.* **2019**, 5, 1900197.
- [37] C.-M. Yang, T.-C. Chen, D. Verma, L.-J. Li, B. Liu, W.-H. Chang, C.-S. Lai, *Adv. Funct. Mater.* **2020**, 30, 2001598.
- [38] L. Chua, *Appl. Phys. A: Mater. Sci. Process.* **2011**, 102, 765.
- [39] R. Waser, R. Dittmann, G. Staikov, K. Szot, *Adv. Mater.* **2009**, 21, 2632.
- [40] X. L. Zhao, J. Ma, X. H. Xiao, Q. Liu, L. Shao, D. Chen, S. Liu, J. B. Niu, X. M. Zhang, Y. Wang, R. R. Cao, W. Wang, Z. F. Di, H. B. Lv, S. B. Long, M. Liu, *Adv. Mater.* **2018**, 30, 1705193.
- [41] X. Yang, Y. C. Fang, Z. Z. Yu, Z. W. Wang, T. Zhang, M. H. Yin, M. Lin, Y. C. Yang, Y. M. Cai, R. Huang, *Nanoscale* **2016**, 8, 18897.
- [42] Y. Shi, X. Liang, B. Yuan, V. Chen, H. Li, F. Hui, Z. Yu, F. Yuan, E. Pop, H.-S. Philip Wong, M. Lanza, *Nat. Electron.* **2018**, 1, 458.
- [43] Z. Wang, T. Zeng, Y. Ren, Y. Lin, H. Xu, X. Zhao, Y. Liu, D. Ielmini, *Nat. Commun.* **2020**, 11, 1510.
- [44] A. Serb, J. Bill, A. Khat, R. Berdan, R. Legenstein, T. Prodromakis, *Nat. Commun.* **2016**, 7, 12611.
- [45] P. M. Sheridan, F. Cai, C. Du, W. Ma, Z. Zhang, W. D. Lu, *Nat. Nanotechnol.* **2017**, 12, 784.
- [46] M. Wang, S. Cai, C. Pan, C. Wang, X. Lian, Y. Zhuo, K. Xu, T. Cao, X. Pan, B. Wang, S.-J. Liang, J. J. Yang, P. Wang, F. Miao, *Nat. Electron.* **2018**, 1, 130.
- [47] Y. Lu, A. Alvarez, C.-H. Kao, J. S. Bow, S. Y. Chen, I. W. Chen, *Nat. Electron.* **2019**, 2, 66.
- [48] I. Boybat, M. L. Gallo, S. R. Nandakumar, T. Moraitis, T. Parnell, T. Tuma, B. Rajendran, Y. Leblebici, A. Sebastian, E. Eleftheriou, *Nat. Commun.* **2018**, 9, 2514.
- [49] A. Bera, H. Peng, J. Lourembam, Y. Shen, X. W. Sun, T. Wu, *Adv. Funct. Mater.* **2013**, 23, 4977.
- [50] P. Maier, F. Hartmann, M. Rebello Sousa Dias, M. Emmerling, C. Schneider, L. K. Castelano, M. Kamp, I. G. E. Marques, V. Lopez-Richard, L. Worschech, S. Hofling, *Appl. Phys. Lett.* **2016**, 109, 023501.
- [51] Y. Zhou, K. S. Yew, D. S. Ang, T. Kawashima, M. K. Bera, H. Z. Zhang, G. Bersuker, *Appl. Phys. Lett.* **2015**, 107, 072107.
- [52] X. J. Zhu, J. H. Lee, W. D. Lu, *Adv. Mater.* **2017**, 29, 1700527.
- [53] L. Chua, *Semicond. Sci. Technol.* **2014**, 29, 104001.
- [54] E. H. Rhoderick, *IEE Proc., Part I: Solid-State Electron Devices* **1982**, 129, 1.
- [55] S. Gao, G. Liu, H. Yang, C. Hu, Q. Chen, G. Gong, W. Xue, X. Yi, J. Shang, R.-W. Li, *ACS Nano* **2019**, 13, 2634.
- [56] J. H. Yoon, S. J. Song, I.-H. Yoo, J. Y. Seok, K. J. Yoon, D. E. Kwon, T. H. Park, C. S. Hwang, *Adv. Funct. Mater.* **2014**, 24, 5086.
- [57] X. Huang, C. Wu, H. Lu, F. Ren, Q. Xu, H. Ou, R. Zhang, Y. Zheng, *Appl. Phys. Lett.* **2012**, 100, 243505.
- [58] Z. Burshtein, J. Levinson, *Phys. Rev. B* **1975**, 12, 3453.
- [59] V. V. Afanas'ev, A. Stesmans, *J. Appl. Phys.* **2007**, 102, 081301.
- [60] G. Q. Bi, M. M. Poo, *J. Neurosci.* **1998**, 18, 10464.
- [61] W. Wang, G. Pedretti, V. Milo, R. Carboni, A. Calderoni, N. Ramaswamy, A. S. Spinelli, D. Ielmini, *Sci. Adv.* **2018**, 4, eaat4752.
- [62] A. Takagi, K. Nomura, H. Ohta, H. Yanagi, T. Kamiya, M. Hirano, H. Hosono, *Thin Solid Films* **2005**, 486, 38.
- [63] T. Kamiya, K. Nomura, H. Hosono, *Phys. Status Solidi A* **2009**, 206, 860.
- [64] T. Kamiya, K. Nomura, M. Hirano, H. Hosono, *Phys. Status Solidi C* **2008**, 5, 3098.
- [65] K. Nomura, T. Kamiya, H. Yanagi, E. Ikenaga, K. Yang, K. Kobayashi, M. Hirano, H. Hosono, *Appl. Phys. Lett.* **2008**, 92, 202117.
- [66] R. B. Pan, J. Li, F. Zhuge, L. Zhu, L. Liang, H. Zhang, J. Gao, H. Cao, B. Fu, K. Li, *Appl. Phys. Lett.* **2016**, 108, 013504.
- [67] S. Jeon, S.-E. Ahn, I. Song, C. J. Kim, U.-I. Chung, E. Lee, I. Yoo, A. Nathan, S. Lee, J. Robertson, K. Kim, *Nat. Mater.* **2012**, 11, 301.
- [68] A. Janotti, C. G. Van de Walle, *Appl. Phys. Lett.* **2005**, 87, 122102.
- [69] H. W. Tan, G. Liu, H. Yang, X. Yi, L. Pan, J. Shang, S. Long, M. Liu, Y. Wu, R.-W. Li, *ACS Nano* **2017**, 11, 11298.